doi:10.1038/nature23006

Three-dimensional magnetization structures revealed with X-ray vector nanotomography

Claire Donnelly[1,2], Manuel Guizar-Sicairos[2], Valerio Scagnoli[1,2], Sebastian Gliga[3], Mirko Holler[2], Jörg Raabe[2] & Laura J. Heyderman[1,2]

In soft ferromagnetic materials, the smoothly varying magnetization leads to the formation of fundamental patterns such as domains, vortices and domain walls[1]. These have been studied extensively in thin films of thicknesses up to around 200 nanometres, in which the magnetization is accessible with current transmission imaging methods that make use of electrons or soft X-rays. In thicker samples, however, in which the magnetization structure varies throughout the thickness and is intrinsically three dimensional, determining the complex magnetic structure directly still represents a challenge[1,3]. We have developed hard-X-ray vector nanotomography with which to determine the three-dimensional magnetic configuration at the nanoscale within micrometre-sized samples. We imaged the structure of the magnetization within a soft magnetic pillar of diameter 5 micrometres with a spatial resolution of 100 nanometres and, within the bulk, observed a complex magnetic configuration that consists of vortices and antivortices that form cross-tie walls and vortex walls along intersecting planes. At the intersections of these structures, magnetic singularities—Bloch points—occur. These were predicted more than fifty years ago[4] but have so far not been directly observed. Here we image the three-dimensional magnetic structure in the vicinity of the Bloch points, which until now has been accessible only through micromagnetic simulations, and identify two possible magnetization configurations: a circulating magnetization structure[5] and a twisted state that appears to correspond to an 'anti-Bloch point'. Our imaging method enables the nanoscale study of topological magnetic structures[6] in systems with sizes of the order of tens of micrometres. Knowledge of internal nanomagnetic textures is critical for understanding macroscopic magnetic properties and for designing bulk magnets for technological applications[7].

Until now, the nanoscale investigation of the internal magnetic structure within films and nanostructures has been possible with various techniques including soft-X-ray[8] and electron[9–11] microscopies, which are limited to investigations of films of thicknesses below approximately 200 nm and 100 nm, respectively, and are thus ideally suited to probe thin-film magnetism in transmission. These techniques have recently been extended towards tomographic imaging[8–11] of three-dimensional patterned[10], rolled or curved structures[8]. The introduction of three-dimensionality provides additional degrees of freedom, and can result in novel properties such as magnetochirality[12] or curvature-induced anisotropy[13].

However, the imaging is limited to thin samples, so new approaches are required in order to image the three-dimensional structure of extended and bulk magnetic systems beyond these limits. Indeed, complex magnetization patterns on this scale still remain to be understood, such as, for example, the surface domain patterns observed in [111] iron whiskers[14]. In addition, direct imaging of the three-dimensional structure of the magnetization is technologically important because the magnetic microstructure determines the performance of soft magnets with high permeability, which are essential for inductive applications such as motors or sensors[1,8], as well as that of permanent magnets, used for energy harvesting and mechanical applications[7]. For example, technologically desired high permeabilities are linked to the nature of domain walls and their displacement.

In this context, an important yet elusive micromagnetic structure is the Bloch point, a singularity in the magnetization that has been predicted to affect both the topology of the magnetization[4] and its behaviour, such as magnetization reversal[2], pinning to the atomic lattice[15] or vortex[16,17] and domain wall dynamics[18].

In terms of the three-dimensional imaging of extended systems, neutron tomographic imaging techniques[19,20] have enabled spatial resolutions of 35–100 μm to be achieved, whereas sub-micrometre spatial resolution had previously been obtained only by using a material-destructive technique[3]. In contrast, hard X-rays offer a combination of high spatial resolution and high penetration depth, making possible nanoscale investigations of samples of the order of tens of micrometres[21], and thus providing a flexible solution to tomographic imaging. With recent progress in high-spatial-resolution hard-X-ray magnetic investigations of micrometre-sized systems[22] and given that hard-X-ray tomography of the electron density of micrometre-sized samples has reached a spatial resolution of 15 nm (ref. 21), the combination of high spatial resolution and high penetration of hard X-rays thus provides a promising method for high-spatial-resolution three-dimensional studies of ferromagnetic systems[13].

One of the key challenges of three-dimensional magnetic investigations concerns the development of an appropriate tomographic algorithm with which to obtain the three-dimensional magnetic vector field. In contrast to traditional tomography, which retrieves a scalar value such as the electron density at each point, for magnetic tomography three separate components of the magnetization must be reconstructed for each individual voxel. So far, this has been achieved in specific samples by making use of the available constraints. For example, with electron tomography the complexity can be reduced through Maxwell's equations (refs 9 and 23). With soft X-rays, the magnetic vector field has been obtained by incorporating prior knowledge of the magnetic properties of the material[8]. Here we combine a dual-axis measurement strategy with a new tomographic reconstruction algorithm to obtain the magnetization vector field with nanoscale spatial resolution, exploiting the high penetration depth of hard X-rays to image a sample with a diameter of several micrometres.

Using hard-X-ray magnetic tomography, we determine the three-dimensional magnetization configuration of a soft $GdCo_2$ (ref. 24) magnetic cylinder of diameter 5 μm. The two magnetic sublattices of the ferrimagnet are strongly coupled antiparallel to each other, leading to an effective soft ferromagnetic behaviour[25]. The investigated sample (insets to Fig. 1a) was cut from a nugget using focused ion beam milling and mounted on top of a tomography pin using a micromanipulator. By measuring at the absorption edge of the magnetic material with

[1]Laboratory for Mesoscopic Systems, Department of Materials, ETH Zurich, 8093 Zurich, Switzerland. [2]Paul Scherrer Institute, 5232 Villigen, Switzerland. [3]SUPA, School of Physics and Astronomy, University of Glasgow, Glasgow G12 8QQ, UK.

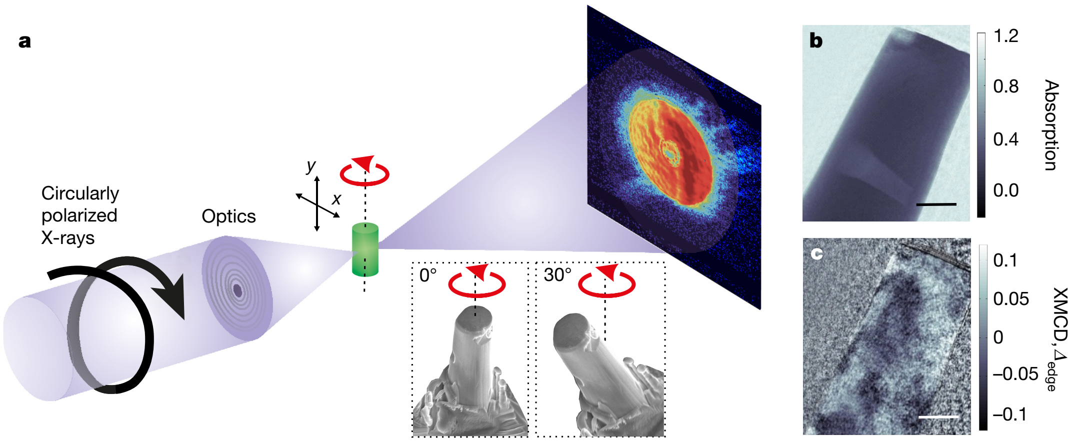

Figure 1 | X-ray magnetic tomography. a, Schematic of setup with circularly polarized X-rays incident on the sample. Ptychographic scans are performed whereby the diffraction pattern is measured in the far field at several sample positions in the x–y plane with mutually overlapping illumination. To have access to all three components of the magnetization, tomographic data are collected for two axes of rotation (see insets showing the $GdCo_2$ pillar, of diameter 5 μm, showing tilt angles $\theta = 0°$ and 30°). **b**, A ptychographic reconstruction of the absorption measured with a single circular polarization contains both electronic and magnetic contrast. **c**, A purely magnetic image can be obtained by taking the difference between images recorded with left and right circularly polarized light and is given as a factor of the difference in absorption across the absorption edge, Δ_{edge} (see Methods)[22]. Scale bars in **b** and **c** represent 2 μm.

circularly polarized X-rays, we can exploit X-ray magnetic circular dichroism (XMCD), which is sensitive to the component of the magnetization parallel to the X-ray beam[26]. A two-dimensional XMCD projection of the pillar (Fig. 1c) already gives an indication that the internal magnetic structure is complex. We next perform magnetic vector tomography to elucidate the details of the three-dimensional internal structure at the nanoscale.

Experimentally, magnetic tomography is performed as shown in Fig. 1a to determine the as-grown magnetization state of the sample. For each axis of rotation, two-dimensional absorption images are recorded using circular left polarized X-rays[27] with hard-X-ray dichroic ptychography[22] for 512 different orientations distributed over 360° with equal angular spacing (see Fig. 1b). The details of the tomographic reconstruction and calculations of the spatial resolution are described in Methods. The spatial resolution was found to range between 97 nm and 127 nm, depending on the direction or plane considered. The direction dependence of the spatial resolution is a result of the m_y component—that is, the component of the magnetization along the long axis of the pillar—receiving effectively less flux owing to the experimental geometry. This estimate of the spatial resolution was confirmed by the fact that we can resolve a magnetic vortex from an antivortex in the x–z plane with a separation of 126 nm (see Methods subsection 'Spatial resolution').

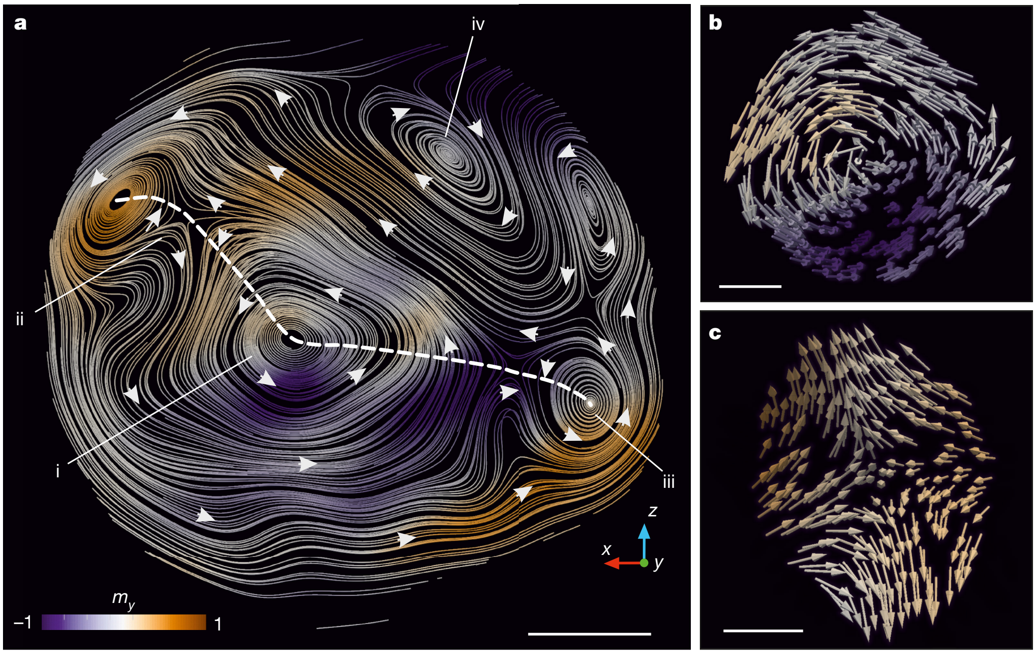

Figure 2 | Axial tomographic slice of the reconstructed magnetization vector field. a, A section taken perpendicular to the long axis of the cylindrical sample is shown, in which the streamlines represent the x–z components of the magnetization and different magnetic structures can be identified. There are anticlockwise vortices, such as (i) and (iii), a clockwise vortex (iv), and antivortices, such as (ii), which occur between two vortices with the same vorticity. **b**, **c**, The three-dimensional magnetic nanostructure of vortex (i) and antivortex (ii), respectively, is shown in more detail. A section of a cross-tie wall consisting of a succession of vortex and antivortex structures is indicated by the dashed white line in **a**. Scale bars represent 1 μm in **a** and 300 nm in **b** and **c**.

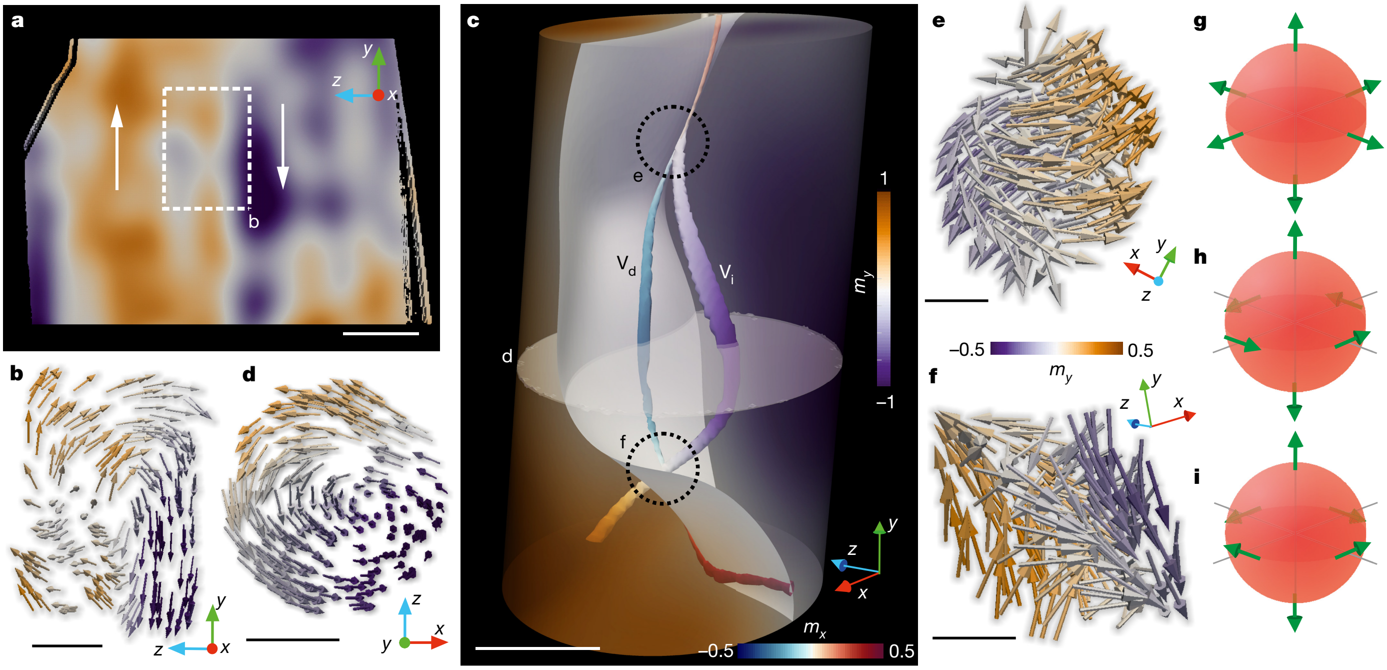

Figure 3 | Details of the reconstructed magnetization. **a**, The y component of the magnetization in a vertical slice through the pillar. Two main large domains of negative (purple) and positive (orange) m_y can be seen, whose magnetic orientation is indicated by the white arrows. **b**, The magnetic configuration of the domain wall in the y–z plane, within the region indicated by a dashed rectangle in **a**. **c**, The domain wall is shown as a white $m_y = 0$ isosurface within a portion of the pillar. The core, V_d, of the vortex wall, coloured by the direction of the magnetization component aligned along the unit vector $\hat{\boldsymbol{x}}$ within the core 16, runs along the domain wall. The magnetic configuration of an axial slice through the portion of the pillar, indicated by the white disk, is given in **d**. The core, V_i, of vortex (i) in Fig. 2, which is part of the cross-tie wall, extends through the length of the pillar and is mapped by an isosurface whose colour represents the magnetization orientation (orange and purple for $+m_y$ and $-m_y$, respectively). Within the volume shown, V_i and V_d intersect at the two circled points e and f. At these points $m_x = m_y = m_z = 0$, corresponding to a magnetic singularity, or Bloch point. While the Bloch points themselves cannot be resolved, the magnetization configuration in their vicinity (within a 125 nm radius) is shown in **e** and **f**. For reference, three possible configurations for Bloch points are shown schematically: **g**, a 'hedgehog', or diverging Bloch point; **h**, a circulating Bloch point; and **i**, a contra-circulating Bloch point (or anti-Bloch point), where the vortex in **h** is replaced by an antivortex. Scale bars represent 1 μm (**a**), 500 nm (**b**–**d**) and 100 nm (**e**, **f**). In **a**–**f** reconstructed experimental data is given, while in **g**–**i** schematic drawings are shown. The three-dimensional structure of Fig. 3c, e and f can be seen in Supplementary Videos 1–3 .

To understand the complex magnetization distribution, we first consider axial slices of the pillar: a 40 nm-thick slice is presented in Fig. 2a with the direction of the magnetization in the x–z plane represented using streamlines whose colour indicates the y component of the magnetization (along the long axis of the pillar). The magnetic configuration contains several inhomogeneous structures, which are magnetostatically favoured despite the resulting increase in the exchange energy. In particular, there is a dense arrangement of magnetic vortices with both negative and positive vorticities (corresponding to the clockwise and anticlockwise curling of the magnetization). The structure of the anticlockwise vortex (i) is shown in detail in Fig. 2b. Between vortices with opposite vorticities, such as (i) and (iv), the magnetization is almost uniform, whereas between vortices with identical vorticities, such as (i) and (iii), the magnetization is inhomogeneous, leading to the formation of antivortices. The detailed magnetic configuration of the antivortex (ii) can be seen in Fig. 2c. The succession of vortex and antivortex structures gives rise to a cross-tie wall across the pillar (a section of which is indicated by the dashed line in Fig. 2a). This cross-tie wall separates regions of opposite magnetization in the plane of the tomographic slice. Unlike in magnetic thin films, the magnetic structures in the bulk are not confined to a single plane. Instead they display a non-zero magnetization component along the axis of the pillar (m_y), which is not limited to the cores of the structures, as is the case in thin films.

Considering the full three-dimensional magnetization configuration surrounding vortex (i) in Fig. 2a, which extends through the height of the pillar, we observe a complex structure owing to the large number of degrees of freedom resulting from the lack of spatial confinement and negligible anisotropy. Our reconstruction reveals two large domains of positive and negative m_y (Fig. 3a), separated by a domain wall extending along the height of the pillar. This domain wall is a vortex wall and intersects the cross-tie wall in Fig. 2. The structure of the vortex wall can be seen from the detailed magnetization vectors for a section of the wall shown in Fig. 3b. In contrast to domain walls in thin films and in high anisotropy materials, which typically extend over a few to tens of nanometres, here the domain wall extends over a few hundred nanometres as expected in an ideal soft ferromagnet in the absence of lateral confinement[28]. The central plane of the domain wall is mapped using the $m_y = 0$ (white) isosurface for a subsection of the pillar in Fig. 3c, and the core, V_d, of the vortex wall can be seen to run along the wall in Fig. 3c (the detailed correspondence between Fig. 2 and Fig. 3a and c is given in Extended Data Fig. 6). The core, V_i, of vortex (i) in Fig. 2 intersects this domain wall at multiple locations, coinciding with the core, V_d, of the vortex wall. At these intersections the polarization, that is, the orientation of the magnetization within both cores, V_i and V_d, reverses. This reversal can be seen in Fig. 3c at point f, where the colour indicates the direction of the magnetisation within the vortex core V_i, which changes from $+m_y$ (orange) to $-m_y$ (purple) on either side of the wall. The polarization of the vortex wall, given by the colour of its core V_d, also reverses from $+m_x$ (red) to $-m_x$ (blue).

At the points of intersection of the core V_i with the domain wall (indicated by circles e and f in Fig. 3c), $m_x = m_y = m_z = 0$, corresponding to a magnetic singularity, or Bloch point. Although such singularities were predicted over fifty years ago[4] and have been studied theoretically, they have so far not been directly observed experimentally. The Bloch point contains a singularity around which the magnetic order is destroyed within a radius of the order of a few lattice constants[15]. The structure of the Bloch point is determined by the magnetization surrounding the singularity on a radius of the order of the exchange length (approximately 5 nm in $GdCo_2$). Here we resolve the three-dimensional magnetization configuration in the vicinity of a pair of singularities, with a spatial resolution of 100 nm, as shown in Fig. 3e and f. The magnetization distribution observed in Fig. 3e is in agreement with the one predicted by micromagnetic simulations around a circulating Bloch point (schematically illustrated in Fig. 3h)[5]. Whereas the prototypical structure of a Bloch point is a 'hedgehog', with the magnetization radially diverging around a central point (Fig. 3g), the observed circulating Bloch point structure (Fig. 3h) is more stable owing to the local magnetic flux closure[5] and as a result the magnetization structure of the Bloch point extends beyond the exchange length (Fig. 3e). For other types of Bloch point, micromagnetic studies have shown that, beyond a radius equal to the exchange length of the material, the magnetization becomes twisted in order to achieve a magnetostatically stable configuration that effectively screens the magnetic monopole charge created by the singularity. Considering that, within the bulk, Bloch points can be created only in pairs, we expect the observed twisted structure in Fig. 3f to correspond to an anti-Bloch point (illustrated in Fig. 3i; see also Extended Data Fig. 3). Such observations constitute a basis for elucidating the relationship between the structure of the magnetization around the Bloch point on the nanometre scale and the complex surrounding magnetic configuration, which spans a sphere tens of nanometres in radius, opening for the first time a possibility for their experimental study.

In this demonstration of hard-X-ray magnetic tomography, we employ dichroic ptychography as an imaging technique that is applicable to a wide variety of materials and sample geometries. Given that we make use of the absorption part of the transmission function, this magnetic tomography technique can in principle be combined with any high-spatial resolution X-ray microscopy technique such as full-field[29] or cone beam propagation microscopy[30], and we envisage that this technique can be implemented at several current and future synchrotrons. With advances in X-ray optics and the advent of upgraded and fourth-generation synchrotrons, the coherent flux available in the hard-X-ray regime can be expected to increase by two to three orders of magnitude in the near future[31,32], bringing hard-X-ray magnetic tomography down to a spatial resolution of the order of 20 nm. In addition, for suitably thin systems, we anticipate that details of three-dimensional spin textures of the order of the exchange length, which are not currently accessible with hard X-rays, could be obtained by applying this method in the soft-X-ray regime.

Online Content Methods, along with any additional Extended Data display items and Source Data, are available in the online version of the paper; references unique to these sections appear only in the online paper.

Received 1 December 2016; accepted 26 May 2017.

1. Hubert, A. & Schäfer, R. *Magnetic Domains: The Analysis of Magnetic Microstructures* (Springer, 1998).
2. Arrott, A. S., Heinrich, B. & Aharoni, A. Point singularities and magnetization reversal in ideally soft ferromagnetic cylinders. *IEEE Trans. Magn.* **15,** 1228–1235 (1979).
3. Shin, S., Schäfer, R. & De Cooman, B. C. Three-dimensional visualization of the magnetic microstructure in bulk Fe-6.6 pct Si. *Metall. Mater. Trans. A* **44,** 4239–4247 (2013).
4. Feldtkeller, E. Mikromagnetisch Stetige und Unstetige Magnetisierungskonfigurationen. *Z. Angew. Phys.* **19,** 530 (1965).
5. Elías, R. G. & Verga, A. Magnetization structure of a Bloch point singularity. *Eur. Phys. J. B* **82,** 159 (2011).
6. Braun, H.-B. Topological effects in nanomagnetism: from superparamagnetism to chiral quantum solitons. *Adv. Phys.* **61,** 1–116 (2012).
7. Gutfleisch, O. *et al.* Magnetic materials and devices for the 21st century: stronger, lighter, and more energy efficient. *Adv. Mater.* **23,** 821–842 (2011).
8. Streubel, R. *et al.* Retrieving spin textures on curved magnetic thin films with full-field soft X-ray microscopies. *Nat. Commun.* **6,** 7612 (2015).
9. Phatak, C., Petford-Long, A. K. & De Graef, M. Three-dimensional study of the vector potential of magnetic structures. *Phys. Rev. Lett.* **104,** 253901 (2010).
10. Phatak, C. *et al.* Visualization of the magnetic structure of sculpted three-dimensional cobalt nanospirals. *Nano Lett.* **14,** 759–764 (2014).
11. Tanigaki, T. *et al.* Three-dimensional observation of magnetic vortex cores in stacked ferromagnetic discs. *Nano Lett.* **15,** 1309–1314 (2015).
12. Hertel, R. Curvature-induced magnetochirality. *Spin* **3,** 134009 (2013).
13. Streubel, R. *et al.* Magnetism in curved geometries. *J. Phys. D* **49,** 363001 (2016).
14. Arrott, A. S. Visualization and interpretation of magnetic configurations using magnetic charge. *IEEE Magn. Lett.* **7,** 1108505 (2016).
15. Andreas, C., Kákay, A. & Hertel, R. Multiscale and multimodel simulation of Bloch-point dynamics. *Phys. Rev. B* **89,** 134403 (2014).
16. Hertel, R. & Schneider, C. M. Exchange explosions: magnetization dynamics during vortex–antivortex annihilation. *Phys. Rev. Lett.* **97,** 177202 (2006).
17. Thiaville, A. *et al.* Micromagnetic study of Bloch-point-mediated vortex core reversal. *Phys. Rev. B* **67,** 094410 (2003).
18. Hertel, R. Ultrafast domain wall dynamics in magnetic nanotubes and nanowires. *J. Phys. Condens. Matter* **28,** 483002 (2016).
19. Kardjilov, N. *et al.* Three-dimensional imaging of magnetic fields with polarized neutrons. *Nat. Phys.* **4,** 399–403 (2008).
20. Manke, I. *et al.* Three-dimensional imaging of magnetic domains. *Nat. Commun.* **1,** 125 (2010).
21. Holler, M. *et al.* High-resolution non-destructive three-dimensional imaging of integrated circuits. *Nature* **543,** 402–406 (2017).
22. Donnelly, C. *et al.* High-resolution hard x-ray magnetic imaging with dichroic ptychography. *Phys. Rev. B* **94,** 064421 (2016).
23. Phatak, C., Beleggia, M. & De Graef, M. Vector field electron tomography of magnetic materials: theoretical development. *Ultramicroscopy* **108,** 503–513 (2008).
24. Burzo, E. Paramagnetic behavior of some rare-earth cobalt compounds. *Phys. Rev. B* **6,** 2882–2887 (1972).
25. Chukazumi, S. in *Physics of Ferromagnetism* Ch. 7.2 (Oxford Univ. Press, 2009).
26. Stoehr, J. & Siegmann, H. *Magnetism: From Fundamentals to Nanoscale Dynamics* Ch. 9 (Springer, 2006).
27. Scagnoli, V. *et al.* Linear polarization scans for resonant X-ray diffraction with a double-phase-plate configuration. *J. Synchrotron Radiat.* **16,** 778–787 (2009).
28. Schäfer, R. Domains in 'extremely' soft magnetic materials. *J. Magn. Magn. Mater.* **215–216,** 652–663 (2000).
29. Chen, Y.-T. *et al.* Full-field hard x-ray microscopy below 30 nm: a challenging nanofabrication achievement. *Nanotechnology* **19,** 395302 (2008).
30. Cloetens, P. *et al.* Holotomography: quantitative phase tomography with micrometer resolution using hard synchrotron radiation x rays. *Appl. Phys. Lett.* **75,** 2912–2914 (1999).
31. Eriksson, M., van der Veen, J. F. & Quitmann, C. Diffraction-limited storage rings—a window to the science of tomorrow. *J. Synchrotron Radiat.* **21,** 837–842 (2014).
32. Thibault, P., Guizar-Sicairos, M. & Menzel, A. Coherent imaging at the diffraction limit. *J. Synchrotron Radiat.* **21,** 1011–1018 (2014).

Supplementary Information is available in the online version of the paper.

Acknowledgements X-ray measurements were performed at the cSAXS beamline at the Swiss Light Source, Paul Scherrer Institut, Switzerland. We thank R. M. Galera for providing and performing magnetic characterizations of the $GdCo_2$ nugget, and S. Stutz and E. Müller for the sample fabrication, as well as K. Metlov, A. Arrott and G. Hrkac for discussions. S.G. was funded by the European Union's Horizon 2020 research and innovation programme under Marie Skłodowska-Curie grant agreement number 708674.

Author Contributions J.R. and L.J.H. conceived the project. C.D., M.G.-S., V.S., M.H. and J.R. designed the experiment. M.H. and J.R. modified the instrument for the 30° tilt measurement. C.D., M.G.-S., V.S., M.H. and J.R. performed the experiment. C.D. and M.G.-S. developed the vector tomography reconstruction algorithm. C.D. performed the data analysis (with support from M.G.-S. and V.S.). C.D., S.G. and J.R. interpreted the magnetic results. C.D., M.G.-S. and S.G. wrote the manuscript with contributions from all authors.

Author Information Reprints and permissions information is available at www.nature.com/reprints. The authors declare no competing financial interests. Readers are welcome to comment on the online version of the paper. Publisher's note: Springer Nature remains neutral with regard to jurisdictional claims in published maps and institutional affiliations. Correspondence and requests for materials should be addressed to C.D. (claire.donnelly@psi.ch), M.G.-S. (manuel.guizar-sicairos@psi.ch) or S.G. (sebastian.gliga@glasgow.ac.uk).

METHODS

Magnetic tomography. The development of the magnetic tomographic algorithm relies on the precise understanding of the angular dependence of the magnetic signal. For the case of X-ray magnetic tomography, we exploit XMCD, for which the signal takes a maximum positive (negative) value when the magnetic moment is parallel (antiparallel) to the X-ray propagation direction and is zero when it is perpendicular. Upon 180° rotation of the sample, the XMCD signal is therefore reversed in sign, and we use this fact to separate the electronic from magnetic contribution in our tomography reconstruction by acquiring data over a 360° angular range, in contrast to the usual 180° range used for conventional tomography. A single measurement, also referred to as a projection, gives the integral of the magnetization component parallel to the X-ray beam, which means that a data set measured around a single rotation axis ($\hat{y}$) perpendicular to the X-ray direction only probes the magnetization in the plane perpendicular to the axis of rotation (m_x, m_z), and not the component of the magnetization parallel to the axis of rotation (m_y). To access all three components of the magnetization, we therefore perform dual-axis tomography, where we record data with the sample at 0° and 30° with respect to the rotation axis (see insets of Fig. 1a). In this manner we record a full data set with access to all three spatial components of the magnetization.

Experimental methods. Magnetic tomography was performed at the cSAXS beamline at the Swiss Light Source, Paul Scherrer Institute, Switzerland, using a high-resolution, interferometrically controlled tomography setup[33]. As found in a previous work, the maximal contrast and signal-to-noise ratio is available with the absorption part of the complex XMCD signal[22]. In addition, the XMCD signal at the Gd L_3 edge is the strongest signal available in the hard-X-ray regime. Therefore, dual-axis magnetic tomography was performed with circularly left polarized light at the Gd L_3 edge with a photon energy of 7.246 keV chosen to maximize the absorption XMCD signal. The two-dimensional absorption images were measured with X-ray ptychography[34–36], a coherent diffractive imaging technique that offers access to the full complex transmission function of the sample with high spatial resolution. In particular, by combining X-ray ptychography with resonant X-rays using a single circular polarization, each image contains both magnetic and electronic contrast[22].

Circularly polarized X-rays were produced as in ref. 22 by converting horizontal linearly polarized X-rays emitted from the undulator source using a 500-μm-thick diamond quarter-wave plate[37]. The degree of circular polarization of the X-rays was determined using a polarization analyser setup[27] and was found to be over 99%, with the phase plate absorbing approximately 65% of the incident light.

For X-ray ptychography we define an X-ray illumination with a diameter of approximately 4 μm on the sample with a combination of a central stop of diameter 40 μm, order sorting aperture of diameter 30 μm, and a Fresnel zone plate with diameter 150 μm and an outermost zone width of 60 nm. To achieve an illumination of 4 μm, the sample was placed 1.18 mm downstream of the focus of the Fresnel zone plate. The total flux incident on the sample is approximately 3×10^8 photons per second. Ptychography scans were performed on a grid of concentric circles[38] with a radial separation of 0.4 μm and with a field of view of 8 μm × 7 μm (351 scanning points) and 13 μm × 9 μm (730 scanning points) for the 0° (not tilted) and 30° tilt angles of the sample, respectively. At each of the scanning points, a diffraction pattern was recorded with an exposure time of 0.2 s on a Pilatus detector[39,40] placed 7.243 m downstream of the sample.

Ptychographic reconstructions were performed using 500 iterations of the difference-map algorithm[35] followed by 200 iterations of maximum likelihood refinement[41,42] using 400 × 400 pixels of the detector, resulting in projections that had a pixel size of 18 nm. An initial guess for the illumination was obtained through a previous ptychography measurement on a strongly scattering test object and, during the reconstruction, both the object and the illumination were iteratively optimized.

The photon energy was calibrated by performing spectroscopic ptychography across the Gd L_3 edge in order to obtain an absorption spectrum that could be compared with reference data[43]. In this way, the energy at which the XMCD signal is maximal was determined. Ptychography scans of the $GdCo_2$ pillar were performed for energies ranging between 7.2025 keV and 7.2815 keV in steps of 1.5 eV as described in ref. 22. The reconstructions were aligned to within a small fraction of a pixel[44] and the absorption part of each complex reconstruction was normalized using a region of air whose transmission should be equal to one. An absorption spectrum was obtained by averaging a section of the image that contains material and plotting these values as a function of energy (see Extended Data Fig. 1). The absorption spectrum was then compared to reference spectra measured on a similar material[43] to determine the energy corresponding to the maximum XMCD signal. The difference in absorption across the absorption edge, Δ_{edge}, is indicated in Extended Data Fig. 1. As in ref. 22, we define the XMCD signal in terms of Δ_{edge}, which on-resonance equates to approximately 10%. For the tomogram of the non-tilted sample, 512 projections were measured with equal angular spacing over 360°. To account for the gaps between detector modules, where we lose part of the diffraction pattern, neighbouring projections were measured using different detector positions[33] and reconstructed together in pairs of scans that share a common illumination function[45]. The entire sample pin was then remounted in the setup at a tilt angle of 30° using a dedicated sample holder and a tomogram with the same tomographic angular resolution measured. Each individual projection had a measurement time of 120 s and 246 s for the 0° and 30° tilt angles, respectively, giving a total time of 52 h for an investigated region of 351 μm^3. The radiation dose applied to the sample during the measurement was 2.8×10^9 Gy.

As a validation for the tomographic reconstruction, two-dimensional XMCD images were measured as described in ref. 22. The images were taken at a photon energy of 7.246 keV with the sample in the tilted geometry (at 30°); for different rotation angles of the sample with respect to the tomographic rotation axis, the sample was rotated in 30° steps from 0° to 150°. The ptychographic scan parameters were the same as those used for the tomogram. For each angle, ten images for each circular polarization (left and right) were aligned[44] and averaged, with each averaged XMCD image requiring a total measurement time of 1 h 40 min. The two-dimensional XMCD images are compared with equivalent projections computed from the reconstructed magnetic tomogram in Extended Data Fig. 2 and show good agreement.

Non-magnetic tomographic reconstruction. To obtain an optimal tomographic reconstruction, the set of projections is first processed and aligned to high precision. For each data set at 0° and 30°, the following postprocessing routine was performed. As a first step, regions of air around the pillar are selected to serve as references in order to normalize the overall transmission, and remove linear and constant offsets to the phase part of the transmissivity[46]. The phase information, which has a higher signal-to-noise ratio than the absorption part, is then used to refine the alignment of the projections following the procedure in ref. 46 and, as a final step, the horizontal alignment is refined based on tomographic consistency[47]. These alignment values are subsequently applied to the complex-valued projections and an electron density tomogram is then obtained from the phase of the projections by applying a modified filtered back-projection that is insensitive to phase wrapping[46]. For the latter, the full range of sample rotation from 0° to 360° can be used because the magnetic contribution cancels for angles θ and $\theta + 180°$.

Magnetic tomographic reconstruction. The scattering factor of a material with a magnetic moment $\boldsymbol{m}(\boldsymbol{r})$ is dependent on both the electronic and magnetic scattering. For the case of circularly polarized light incident on a ferromagnetic sample in the limit of resonant small angle scattering[48], the scattering factor can be approximated to:

$$f = f_{\mathrm{c}} \pm i f_{\mathrm{m}} \hat{\boldsymbol{z}} \cdot \boldsymbol{m}(\boldsymbol{r})$$

where f_{c} is the electronic scattering factor, f_{m} is the magnetic scattering factor, $\boldsymbol{r} = (x, y, z)$ is the Cartesian coordinate vector, and the unit vector $\hat{\boldsymbol{z}}$ is the direction of propagation of the X-rays. The magnetic signal that we measure with XMCD is therefore proportional to the component of the magnetization parallel to the X-ray beam. Around one rotation axis $\hat{\boldsymbol{y}}$, the measurement is therefore sensitive only to the components of magnetization in the x–z plane perpendicular to the axis of rotation, m_x and m_z. The projected signal as a function of tomographic angle for a single circular polarization can be described as:

$$P_{\varphi}(x, y) = \int [f_{\mathrm{c}}(\boldsymbol{r}') + A(m_x(\boldsymbol{r}')\sin\varphi + m_z(\boldsymbol{r}')\cos\varphi)]\mathrm{d}z$$

where $\boldsymbol{r}'$ is the Cartesian coordinate vector rotated by an angle φ, A is a constant that relates the XMCD signal to the magnetization, and φ is the rotation angle of the sample about the rotation axis $\hat{\boldsymbol{y}}$ with respect to the X-ray beam propagation direction.

A gradient-based iterative optimization routine was used to retrieve $m_x(\boldsymbol{r})$ and $m_z(\boldsymbol{r})$ along with the non-magnetic tomogram for each of the two tomographic measurements (with tilt angles $\theta = 0°$ and $\theta = 30°$), by minimizing an error metric between projections of the reconstructed data set with the measured projections.

The two electron density tomograms, obtained as detailed in Methods subsection 'Non-magnetic tomographic reconstruction', were registered to each other using Avizo software (https://www.fei.com/software/avizo-for-materials-science/), which results in an affine transformation matrix relating the reconstructions of the pillar at 0° and 30° tilt to each other. The magnetic reconstructions are then combined using this affine transformation matrix by solving a system of linear simultaneous equations for each voxel to obtain the three-dimensional magnetization vector field. As a last step, a three-dimensional Hanning low-pass filter was used on each magnetic component to remove high-frequency noise. The open-source software Paraview (https://www.paraview.org/) was used to visualize and map the magnetic configuration of the sample.

Here we reconstruct a value of the XMCD signal on-resonance, which is proportional to the saturation magnetization of the material. In Figs 2 and 3 and Extended Data Fig. 6, all components of the magnetization are normalized to a known value of the XMCD signal that corresponds to the saturation magnetization, m_s, of the sample. As a result, the reconstructed magnetization is given as a factor of the saturation magnetization, with ± 1 corresponding to $\pm m_s$.

Spatial resolution. The spatial resolution of the electron density tomograms was calculated as follows: the data were separated into two independent data sets with twice the angular spacing between tomographic projections. From these data sets, two independent tomograms were computed[33] and the spatial resolution estimated using Fourier shell correlation (FSC) with the half-bit criterion[49]. The spatial resolution was estimated to be 25 nm and 33 nm for the straight and tilted electron density tomograms, respectively.

For the magnetization vector field, two complementary measurement techniques were employed: FSC and the resolution of nearby structures.

Fourier shell correlation. We obtain an estimate for the spatial resolution of the reconstructed magnetization vector field by separating the data sets into two as above, and computing two three-dimensional reconstructions of the magnetization vector field. We estimate the spatial resolution of each scalar magnetic component using FSC and find them to be 195 nm, 250 nm and 196 nm, for the m_x, m_y and m_z components, respectively. Features in a vector field are often identified from the amplitude or direction of the vector, which are calculated via a nonlinear combination of the individual components. To estimate the spatial resolution of the vector field, we calculate the FSC curve for the absolute value of the magnetization in each of three perpendicular planes (see Extended Data Fig. 5), that is $|m_{xy}| = \sqrt{m_x^2 + m_y^2}$ for the x–y plane, and likewise for the x–z and the y–z planes, for which we find values of 125 nm, 97 nm and 127 nm, respectively.

The slightly different values of the spatial resolution corresponding to different directions, or planes, can be explained by considering the geometry of the experimental setup: the m_y component is not probed in the first measurement series with the long axis of the pillar parallel to the rotation axis, and it is only probed in the tilted geometry in which the long axis of the pillar is at an angle of 30° with respect to the rotation axis. In contrast, the m_x and m_z components are probed in both geometries, and in total effectively receive a 3.73 times higher contribution to the signal. As the scattering signal is proportional to the fourth power of the smallest measurable feature size[50], we expect the ratio of the spatial resolutions of m_y to m_x and m_z to be approximately $\sqrt[4]{3.73} = 1.39$, which results in an asymmetry (directional dependence) in the spatial resolution that depends on the plane in which the spatial resolution is calculated.

Resolution of nearby structures. Features of the magnetization were identified using the absolute value of the magnitude of the magnetization vector field. For a vortex, this value is considered in the plane of the vortex $|m_{xz}| = \sqrt{m_x^2 + m_z^2}$. Within the core of the vortex, the magnetization tilts out of the plane, so that the centre of the vortex core can be located by determining the local minimum of $|m_{xz}|$.

We consider the case of a vortex–antivortex pair separated by a decreasing distance as a function of height in Extended Data Fig. 4a–c, where the magnetization direction is given by streamlines. In Extended Data Fig. 4d–f we show $|m_{xz}|$ for three consecutive axial slices, separated by 18 nm, where the centre of the core of the vortices and antivortices are seen as minima $|m_{xz}| = 0$. By considering both the direction (Extended Data Fig. 4b) and magnitude (Extended Data Fig. 4e) of the magnetization, we are able to resolve individual magnetic structures laterally separated by 126 nm (Extended Data Fig. 4b, e and h), in agreement with the FSC calculations. We note that the measured separation is larger than the calculated spatial resolution: this is due to the actual size of the vortex and antivortex cores, which are expected to be of the same order, or slightly larger, than the lateral spatial resolution.

Data availability. The data that support the findings of this study are available from corresponding author C.D. upon reasonable request.

Code availability. Details of the reconstruction algorithm are available from corresponding author C.D. upon reasonable request.

33. Holler, M. *et al.* X-ray ptychographic computed tomography at 16 nm isotropic 3D resolution. *Sci. Rep.* **4,** 3857 (2014).
34. Rodenburg, J. M. *et al.* Hard-x-ray lensless imaging of extended objects. *Phys. Rev. Lett.* **98,** 034801 (2007).
35. Thibault, P. *et al.* High-resolution scanning x-ray diffraction microscopy. *Science* **321,** 379–382 (2008).
36. Tripathi, A. *et al.* Dichroic coherent diffractive imaging. *Proc. Natl Acad. Sci. USA* **108,** 13393–13398 (2011).
37. Giles, C. *et al.* Energy-dispersive phase plate for magnetic circular-dichroism experiments in the X-ray range. *J. Appl. Cryst.* **27,** 232–240 (1994).
38. Dierolf, M. *et al.* Ptychographic X-ray computed tomography at the nanoscale. *Nature* **467,** 436–439 (2010).
39. Henrich, B. *et al.* PILATUS: A single photon counting pixel detector for X-ray applications. *Nucl. Instrum. Meth. A* **607,** 247–249 (2009).
40. Kraft, P. *et al.* Characterization and calibration of PILATUS detectors. *IEEE Trans. Nucl. Sci.* **56,** 758–764 (2009).
41. Guizar-Sicairos, M. & Fienup, J. R. Phase retrieval with transverse translation diversity: a nonlinear optimization approach. *Opt. Express* **16,** 7264–7278 (2008).
42. Thibault, P. & Guizar-Sicairos, M. Maximum-likelihood refinement for coherent diffractive imaging. *New J. Phys.* **14,** 063004 (2012).
43. Bouchenoire, L. *et al.* Performance of phase plates on the XMaS beamline at the ESRF. *J. Synchrotron Radiat.* **10,** 172–176 (2003).
44. Guizar-Sicairos, M., Thurman, S. T. & Fienup, J. R. Efficient subpixel image registration algorithms. *Opt. Lett.* **33,** 156–158 (2008).
45. Guizar-Sicairos, M. *et al.* High-throughput ptychography using Eiger: scanning X-ray nano-imaging of extended regions. *Opt. Express* **22,** 14859–14870 (2014).
46. Guizar-Sicairos, M. *et al.* Phase tomography from x-ray coherent diffractive imaging projections. *Opt. Express* **19,** 21345–21357 (2011).
47. Guizar-Sicairos, M. *et al.* Quantitative interior x-ray nanotomography by a hybrid imaging technique. *Optica* **2,** 259–266 (2015).
48. Hannon, J. P. *et al.* X-ray resonance exchange scattering. *Phys. Rev. Lett.* **61,** 1245–1248 (1988).
49. van Heel, M. & Schatz, M. Fourier shell correlation threshold criteria. *J. Struct. Biol.* **151,** 250–262 (2005).
50. Howells, M. R. *et al.* An assessment of the resolution limitation due to radiation-damage in x-ray diffraction microscopy. *J. Electron Spectrosc. Relat. Phenom.* **170,** 4–12 (2009).

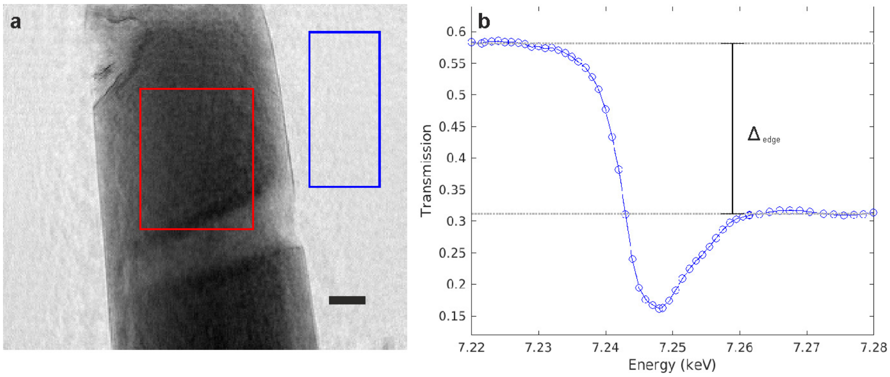

Extended Data Figure 1 | Transmission spectrum obtained with spectroscopic ptychography. a, Absorption part of a ptychographic reconstruction of the pillar measured at 7.203 keV. Regions of air and material are highlighted by the blue and red boxes, respectively. These regions were used to obtain the transmission of the sample at different energies. Such images were measured for a range of energies between 7.203 keV and 7.282 keV in steps of 1.5 eV. **b**, The transmission spectrum obtained from the range of images is shown, and the difference in absorption across the absorption edge, Δ_{edge}, is indicated.

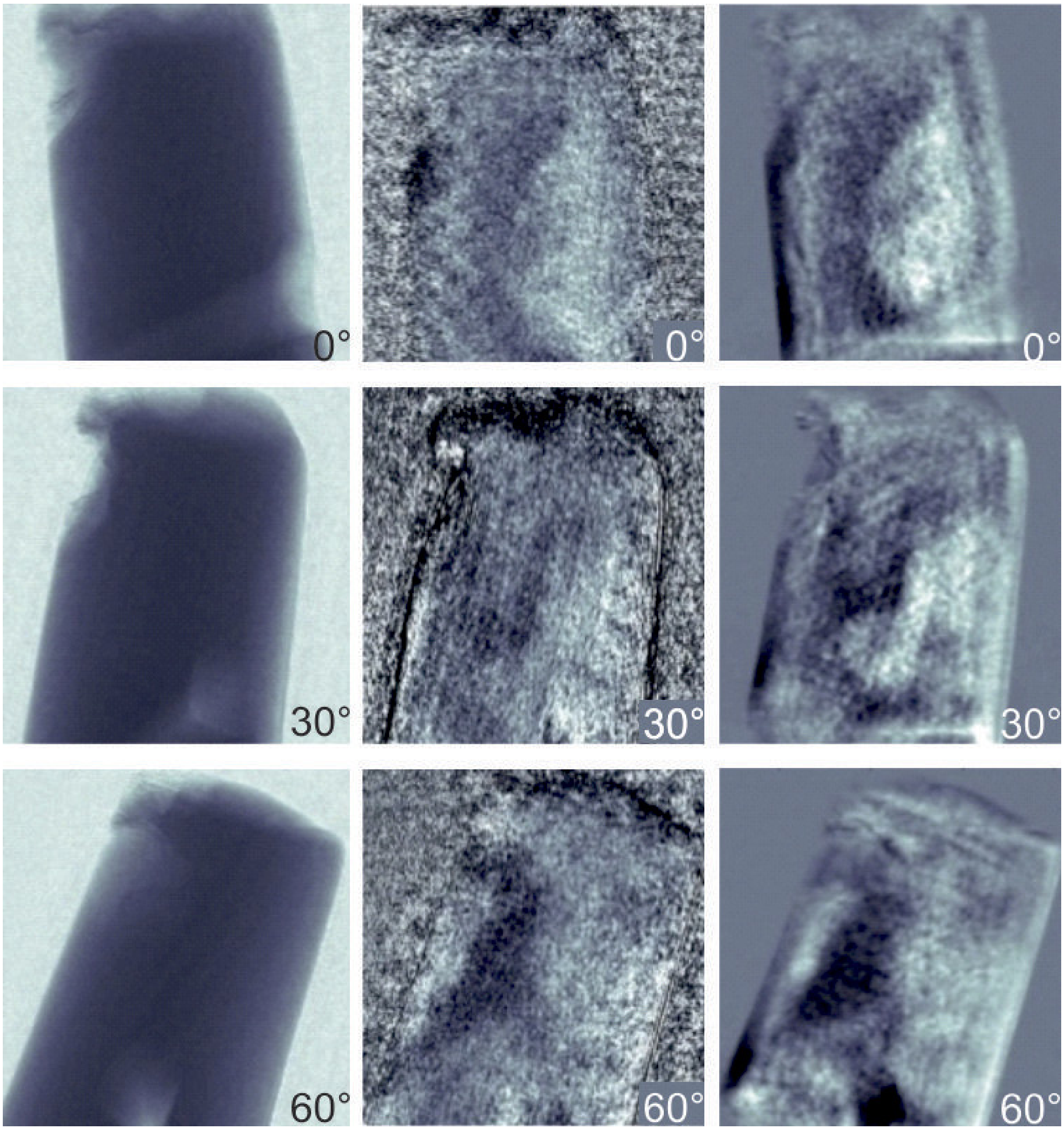

Extended Data Figure 2 | Validation of the magnetic reconstruction. Single polarization images for different angles about the rotation axis (0°, 30° and 60°) in the 30° tilt geometry are shown in the left-hand column. In the central column, XMCD projections obtained by taking the difference between images measured with circular left and right polarization are given, which are the integrals of the magnetic component along the path of the X-ray beam. The equivalent projections obtained from the reconstructed magnetic tomogram are given in the right-hand column. When we compare the images in the central and right columns, the contrast and projection of the magnetization match well. This good agreement provides a validation for the magnetic reconstruction.

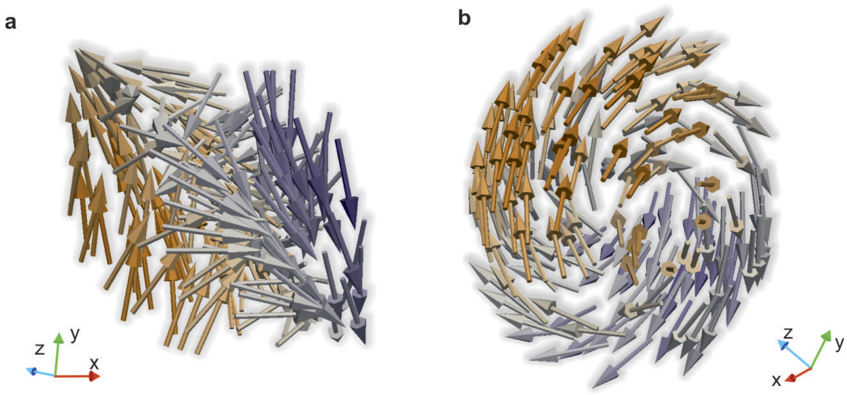

Extended Data Figure 3 | Structure of the magnetization surrounding the singularity shown in Fig. 3f. a, View parallel to the plane of the domain wall shown in Fig. 3c; **b**, view perpendicular to the plane of the domain wall shown in Fig. 3c. The observed magnetic structure does not show a one-to-one correspondence to any of the Bloch point configurations in Fig. 3g–i. While circulating Bloch points have been shown to minimize the magnetostatic energy as result of their swirling magnetization, this is not the case for other Bloch point configurations, where the magnetization in the vicinity of the singularity is predicted to deform in order to minimize the magnetostatic energy. We therefore attribute the structure above to the redistribution of the magnetization in order to screen the magnetostatic charge associated with the monopole generated by the diverging magnetization at the Bloch point.

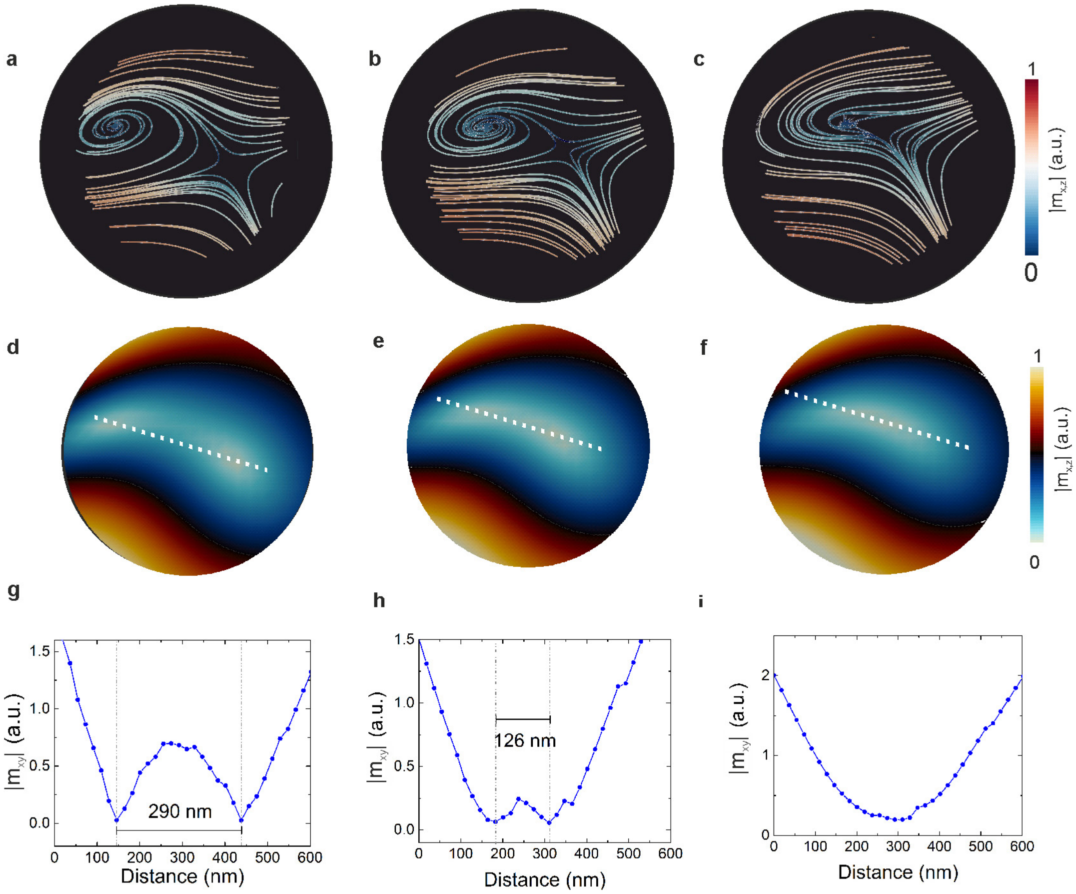

Extended Data Figure 4 | Estimation of the spatial resolution obtained by resolving nearby structures. a–c, Streamlines showing the direction of the magnetization for three x–z slices at heights of 0 nm (midway through the pillar), +20 nm and +40 nm. A vortex–antivortex pair draw closer together as the height increases until they merge and can barely be resolved. **d–f**, The absolute value of the magnetization $|m_{xz}| = \sqrt{m_x^2 + m_z^2}$ is shown for the same areas as **a–c**, where the cores of the vortex and antivortex are minima. **g–i**, The $|m_{xz}|$ line profiles along the dotted lines in **d–f**, where we show that we are able to resolve features in the vector field that are separated by approximately 126 nm (**h**), the structure of which can be seen clearly in **b**, whereas in **i** the two structures can no longer be resolved.

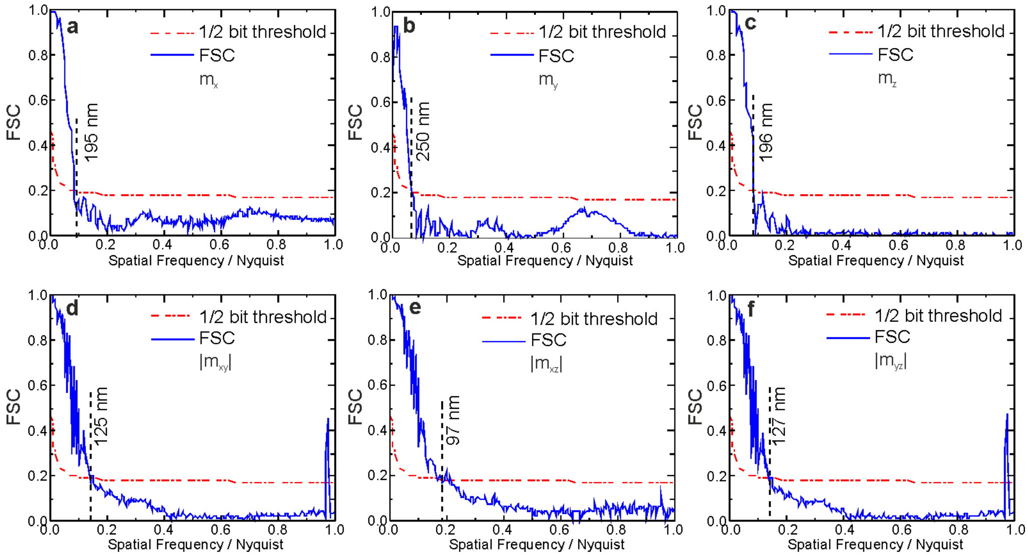

Extended Data Figure 5 | Estimation of the spatial resolution using FSC. a–c, The spatial resolution of the single components of the magnetization vector— m_x (**a**), m_y (**b**) and m_z (**c**)—are found to be 195 nm, 250 nm and 196 nm, respectively. The spatial resolution of m_y is lower because of lower sampling resulting from the experimental geometry, as explained in the text. **d–f**, To estimate the spatial resolution of the vector field, the FSC values are calculated for $|m_{xy}|$ (**d**), $|m_{xz}|$ (**e**) and $|m_{yz}|$ (**f**) to be 125 nm, 97 nm and 127 nm, respectively. The x–y and y–z planes exhibit lower spatial resolution, owing to the low sampling of m_y caused by the experimental geometry.

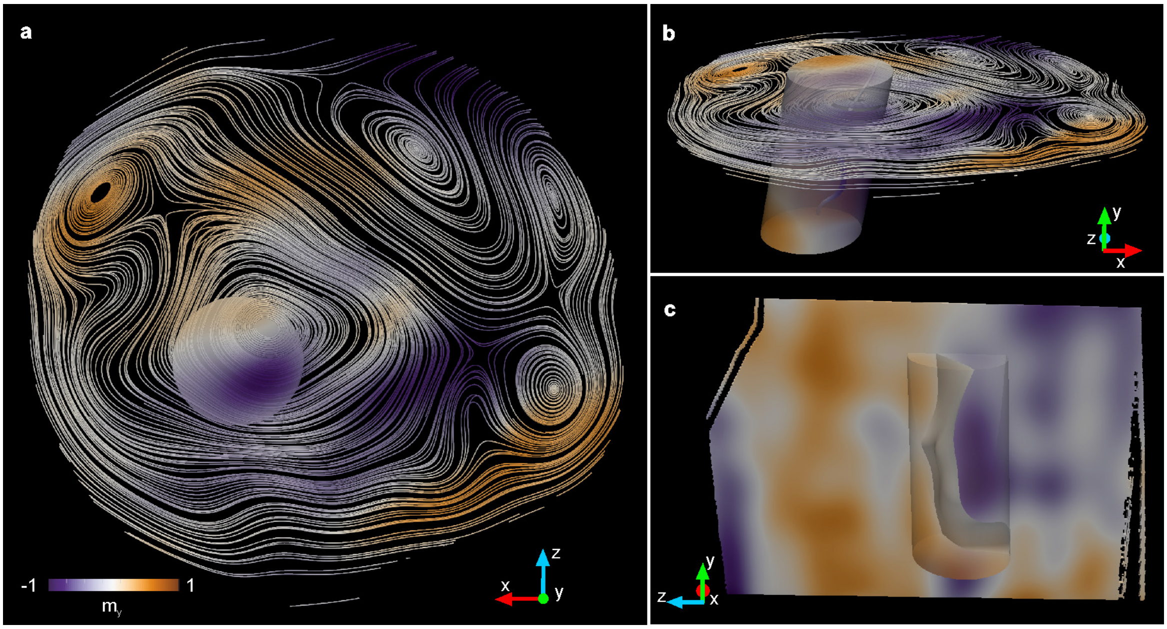

Extended Data Figure 6 | The correspondence of the three-dimensional region in Fig. 3c with the axial slice of Fig. 2a. a, From above; **b**, from the side. The core of vortex (i) is mapped with an isosurface in **b**. The relative positions of the slice in Fig. 3a and the three-dimensional region in Fig. 3c are given in **c**.